# Near-atomic-scale mapping of electronic phases in rare earth nickelate superlattices

*Bernat Mundet, Claribel Domínguez, Jennifer Fowlie, Marta Gibert, Jean-Marc Triscone and Duncan T. L. Alexander*

## SUPPORTING INFORMATION

This file contains additional information about:

1. Specimen preparation and microscope information
2. STEM-EELS acquisition conditions
3. Additional EELS information
    a. Identifying the distinct layers in the O *K* spectrum images
    b. Original raw data
    c. Spectral comparison between the individual layers of the $(30,30)_2$ SL
    d. Mapping the width (FWHM) of the Ni $L_3$ peak

## 1.- Specimen preparation and microscope information

STEM specimens were prepared by mechanical tripod polishing, followed by argon ion beam milling to electron transparency with a Gatan PIPS II. A milling energy of 3 kV is initially used for a few hours, which is then reduced down to 0.5 kV until a small hole is created at the specimen's interface. The STEM data were acquired using a double-aberration-corrected FEI (Thermo Fisher Scientific) Titan Themis 60-300 microscope located at the Interdisciplinary

Centre for Electron Microscopy (CIME), École Polytechnique Fédérale de Lausanne (EPFL) operated either at 200 or 300 kV high tension. The microscope is equipped with a high brightness field-emission gun (X-FEG) with monochromator, a double-aberration-corrector (CEOS-Gmbh) and a Gatan GIF Quantum ERS EELS spectrometer and energy filter.

## 2.- STEM-EELS acquisition conditions

In this section we provide a detailed description of the acquisition conditions that were used to obtain the STEM and STEM-EELS data. The STEM-EELS spectrum image (SI) datasets were acquired with the Gatan GIF Quantum ERS spectrometer using the following conditions: a collection semi-angle of ~47 mrad, a GIF entrance aperture of 2.5 mm, a vertical binning of 130 channels, high-quality read out mode, 16x16 subpixel scanning option activated, ~0.1 s (high-loss) and ~1 ms (low-loss) acquisition times per pixel, 0.1 eV/channel energy dispersion and 2048 channels. A dual EELS configuration was used, which covers the spectral regions of ~ –20 – 185 eV for the low-loss region and 450 – 655 eV for the O *K* edge data or 810 – 1010 eV for the Ni *L* edge high-loss data. In addition to the "limiting" pixel size of 3.5–4 Å for the ~80 pA probe current discussed in the main text, we also observed that beam damage during SI acquisition was significantly reduced when operating the microscope at 200 kV instead of 300 kV. After initial spectrometer tuning using the zero-loss peak, the spectrometer FX focus is then fine-tuned such that the studied fine structure is properly focused. For the O *K* edge analysis, we correct the spectral shift instabilities occurring during SI acquisition by re-aligning the zero-loss peak position to 0 eV for all of the pixels in their low-loss spectra and applying resulting offsets to the high-loss SI. However, this approach is not usable when the Ni *L* edge is properly focused since the zero-loss peak is significantly defocused. In this case, we use the central position of the Ni $L_2$ peak (which should not change between superlattices at a given temperature) as a reference to correct the small spectral offsets between distinct SIs. Another

important parameter, which in part determines the energy resolution of the experiment, is the EEL spectral energy dispersion. In general, better defined fine structures are obtained when increasing the energy dispersion, thus reducing the channel width, although this also constrains the overall spectral range covered by the detector. However, the number of detected electrons per channel also decreases when increasing the dispersion, which can be problematic in low-dose experiments where the output signal is close to the background noise. For the aforementioned conditions, we found that a 0.1 eV/channel dispersion is a good compromise between energy resolution and signal-to-noise ratio (SNR).

Concerning the setup of the monochromated probe, we used a monochromator excitation of 300 V, a circular C1 aperture in the monochromated dispersion plane of 0.5 μm diameter, a spot size number of 13, and a 30 μm diameter C3 aperture. The probe convergence semi-angle for this configuration is ~17 mrad, and the probe size ~1.1–1.2 Å. Using a high spectral dispersion of 0.01 eV/channel this gave a zero-loss peak full width half maximum of ~0.225 eV. Energy resolution reduces to 0.4 eV when using the 0.1 eV/channel energy dispersion of the SI acquisition.

The data processing was done with the Gatan Digital Micrograph software (GMS 3.2). No principal component analysis (PCA) was used for the displayed the O *K* and Ni *L* edge fine-structures. However, we did use a PCA code in Python scripting[1] to minimize the random noise of the acquired EELS-SI datasets when mapping the insulating/metallic regions. This has to be done to improve the signal-to-noise ratio of each individual pixel EEL spectrum in order to ensure good Gaussian profile fitting in all of them.

Each high-resolution high-angle annular dark-field (HAADF) image of the studied superlattices (SLs) results from a stack of 24 individual images (each one scan rotated clockwise by 90º with respect to the previous one) acquired consecutively in the same film region, with dwell times of 0.5 μs/pixel. These 24 images are aligned afterwards with the

SmartAlign plug-in for GMS, which corrects the image drift and the linear and non-linear scan distortions as well.[2,3] For the acquisition of these images, the microscope was operated at 300 kV, using a probe convergence semi-angle of ~20 mrad, a probe current of around 40 pA, and images recorded using a Fischione photomultiplier tube detector with collection semi-angles of ~50.5 – 200 mrad. The final aligned and averaged images typically have a resolution of < 0.7 Å.

## 3.- Additional EELS information

### a) Identifying the distinct layers in the O *K* spectrum images (SI)

To extract the O *K* edge information characteristic of each specific nickelate layer, we have to be capable of associating each pixel to its corresponding layer. This is straightforward when evaluating the Ni *L* edge, since the Nd *M* edge is also present within the measured spectral range. However, this is more problematic for the O *K* edge, since no additional peaks associated to either the Sm or Nd cations are located close to the O *K* edge (530 eV). Therefore, one has to use other approaches, such as looking for other edges or acquiring X-ray energy dispersive spectra simultaneously. In our case, we have used the Sm/Nd *N* edge located at around 135 – 140 eV, which is present within the spectral region of the low-loss SI. Note that the low-loss SI is acquired together and near-simultaneously with the high-loss SI containing the O *K* edge, by using the dual EELS mode. Accordingly, the spatial positions associated to all pixels in both SIs are analogous. The correctness of this Sm/Nd *N* edge approach is demonstrated in Fig. S1 where we show SI data in which the high-loss spectrum instead contains the Ni *L* and Nd *M* edges (~810 – 1010 eV spectral range), such that the latter can be used for result correlation. In (a) we show the Nd and Sm *N* edges (solid lines) in the low-loss spectra, acquired in distinct positions of the $(5,5)_{10}$ SL corresponding to either the $NdNiO_3$ (red) or $SmNiO_3$ (green) layers. This edge is composed of a main peak located at around 135 eV (Nd) or 140 eV (Sm) (solid

vertical lines), and a secondary peak that, depending on the cation, is either located before (Nd) or after (Sm) the main peak. The observed fine structures are similar to those associated to either $Nd_2O_3$ or $Sm_2O_3$ reference compounds (dashed lines) extracted from the EELS atlas reference book,[4] which is an additional clear indication that the degree of intermixing in these SLs is very limited. By fitting the main peak to a Gaussian profile, and then tracking its central position across the SLs, we can effectively distinguish between both nickelate layers, as shown in the colored map of Fig S1 (b) (right panel). This map is in very good agreement with the Nd map (middle panel) generated with the Nd *M* edge signal (as contained within the same dual EELS dataset), thus confirming the validity of this approach when instead applied to the O *K* edge dual EELS datasets.

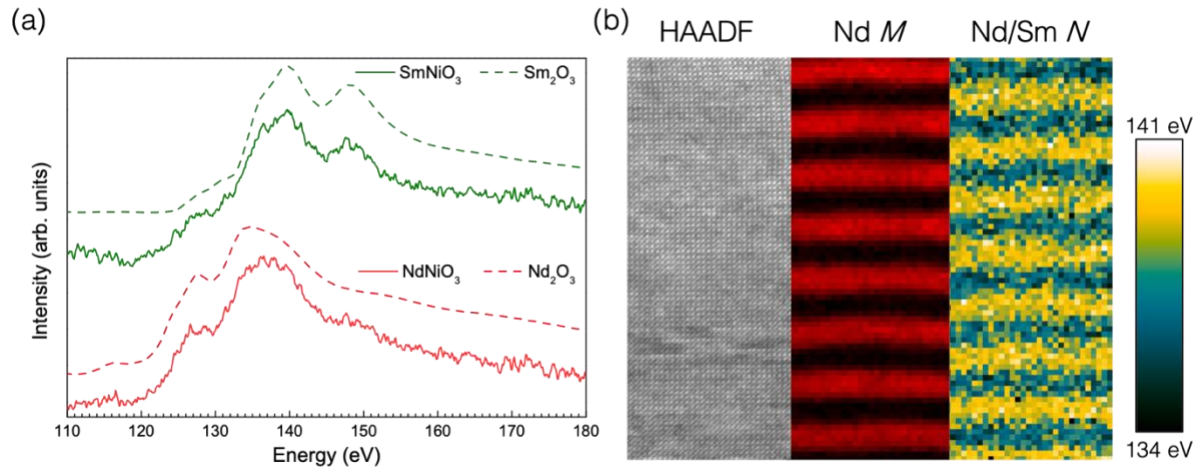


**Figure S1.** (a) Experimental Nd (solid red line) and Sm (solid green line) *N* edges respectively acquired from either the $NdNiO_3$ or $SmNiO_3$ layers of the $(5,5)_{10}$ SL. Their fine structures are compared to the Nd/Sm *N* edges of $Nd_2O_3$ and $Sm_2O_3$ reference compounds. (b) From left to right: HAADF image, Nd compositional map generated from the Nd *M* edge and Sm/Nd *N* main peak position. Both kinds of compositional map match perfectly.

## b) Original raw data

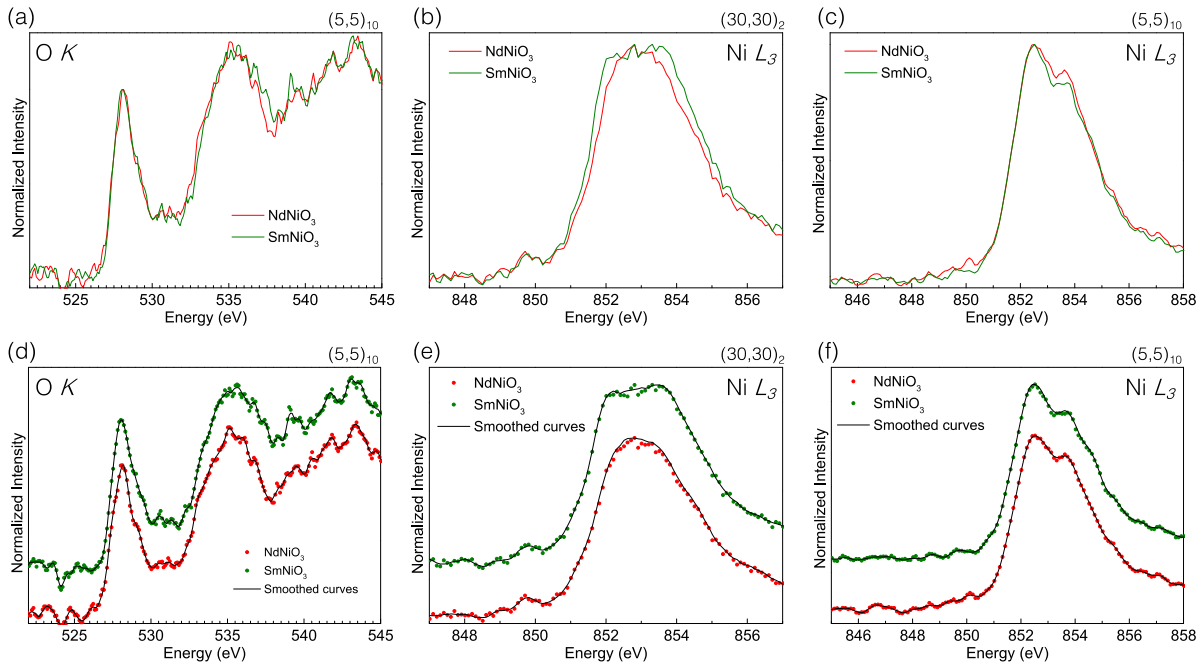


**Figure S2.** Direct comparison of the smoothed EEL spectra that are presented in the main text to the original raw background-subtracted spectra. Raw (background-subtracted) data for the (a) O *K* edge of the $(5,5)_{10}$ SL and Ni $L_3$ peak of the (b) $(30,30)_2$ and (c) $(5,5)_{10}$ SL. The spectra have been normalized to the maximum intensity of either (a) the O *K* edge pre-peak or the (b, c) Ni $L_3$ peak. The curves shown in (a–c) are represented as solid dots in (d–f), and then superposed with their smoothed curves (solid black lines), which are displayed in the main text, for their comparison. For clarity, the curves are shifted along the vertical axis. The O *K* edge associated to the $(30,30)_{10}$ SL is not shown, because no smoothing was used in this case.

## c) Spectral comparison between the individual layers of the $(30,30)_2$ SL

All the O *K* and Ni *L* edges that are shown in the main manuscript result from the integration of EEL spectra from several pixels located at the corresponding $NdNiO_3$ or $SmNiO_3$ layers. Since the shape modulations of the O *K* and Ni *L* edges observed in the $(30,30)_2$ SL are rather small, in order to verify the interpretation of our results, we have also assessed the data obtained from each individual layer in this particular SL. In Fig. S3 (a) we show a HAADF image (left panel) and corresponding Sm/Nd compositional map obtained from the $(30,30)_2$ SL. The

arrows indicate the layers at which the distinct O *K* and Ni *L* edge spectra are obtained, which are shown in Fig. S3 (b) and (c), respectively.

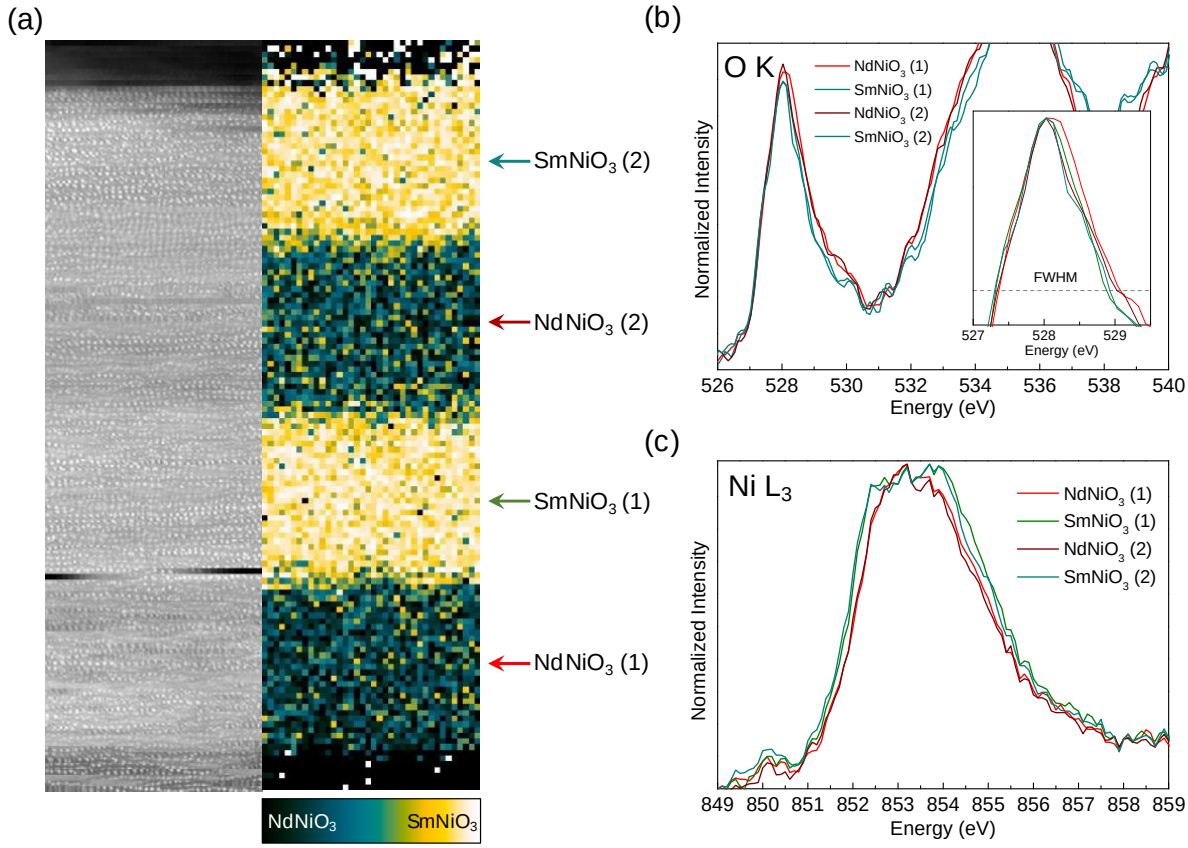


**Figure S3.** (a) HAADF image (left panel) of a $(30,30)_2$ SL and associated Sm/Nd chemical map generated from the relative shift of the Sm/Nd *N* edge. The arrows point to the distinct layers from which the spectra shown in (b) and (c) are obtained. (b) O *K* edge spectra obtained from the distinct layers of the $(30,30)_2$ SL. The spectra are normalized to the main peak maximum intensity after background subtraction. In the inset we show an amplified view of the normalized O *K* pre-peak. (c) Ni $L_3$ peak obtained from the distinct layers of the $(30,30)_2$ SL, normalized to their maximum intensity. Red colors are associated to the distinct $NdNiO_3$ layers, whereas the green colors represent the $SmNiO_3$ ones.

From the O *K* edge spectra, displayed in (b), we can identify that the drop in the pre-peak area and its concomitant pre-peak narrowing (inset) occur in both of the $SmNiO_3$ layers of this SL. Similarly, from the Ni *L* edge spectra, we can also distinguish that the broadening of the Ni $L_3$ peak and the concomitant shift of peak A towards lower energies also occur in both of these $SmNiO_3$ layers. These results confirm that, even though the observed changes are at the

edge of the attainable energy resolution, they are representative of the studied materials and reproducible.

### d) Mapping the width of the Ni $L_3$ peak

In order to rule out the possibility that the mapped spectral shifts of the Ni $L_3$ peak depending on electronic state (Fig. 5 in main text) are actually caused by instabilities in the spectral energy offset, we have also analyzed the broadening of the Ni $L_3$ peak across the two studied SLs. To do so, we use a Gaussian profile fitting to extract the Ni $L_3$ width in all pixels of both SIs. While this fitting may have a certain inaccuracy deriving from the varied splitting of the Ni $L_3$, it is a straightforward approach that gives qualitative insights. For instance, in Fig. S4 (a) we display the Nd chemical map (left panel), the peak A position (middle panel, as shown in Fig. 5 of main text) and the Ni $L_3$ width evolution (right panel) across the $(30,30)_2$ SL. It is clearly seen that in those regions ($SmNiO_3$ layers) where peak A shifts to lower energies, the Ni $L_3$ peak also becomes broader (and vice-versa), which agrees well with the fact these regions are an insulating phase compared to the metallic $NdNiO_3$ layers. Further, when we repeat the same analysis on the $(5,5)_{10}$ SL, as shown in Fig. S4 (b), this Ni $L_3$ peak broadening modulation is no longer observed. Instead, the Ni $L_3$ width remains constant across the whole SL, in agreement with the uniformly metallic nature of the layers across this SL. Note that the changes identified at the bottom and top regions of the films are due to the appearance of the La *M* edge signal in the spectra, which is strongly overlapped with the Ni *L* edge. This signal comes either from the $LaAlO_3$ substrate at the bottom or from some $LaAlO_3$ re-deposition at the top caused by the ion milling process.

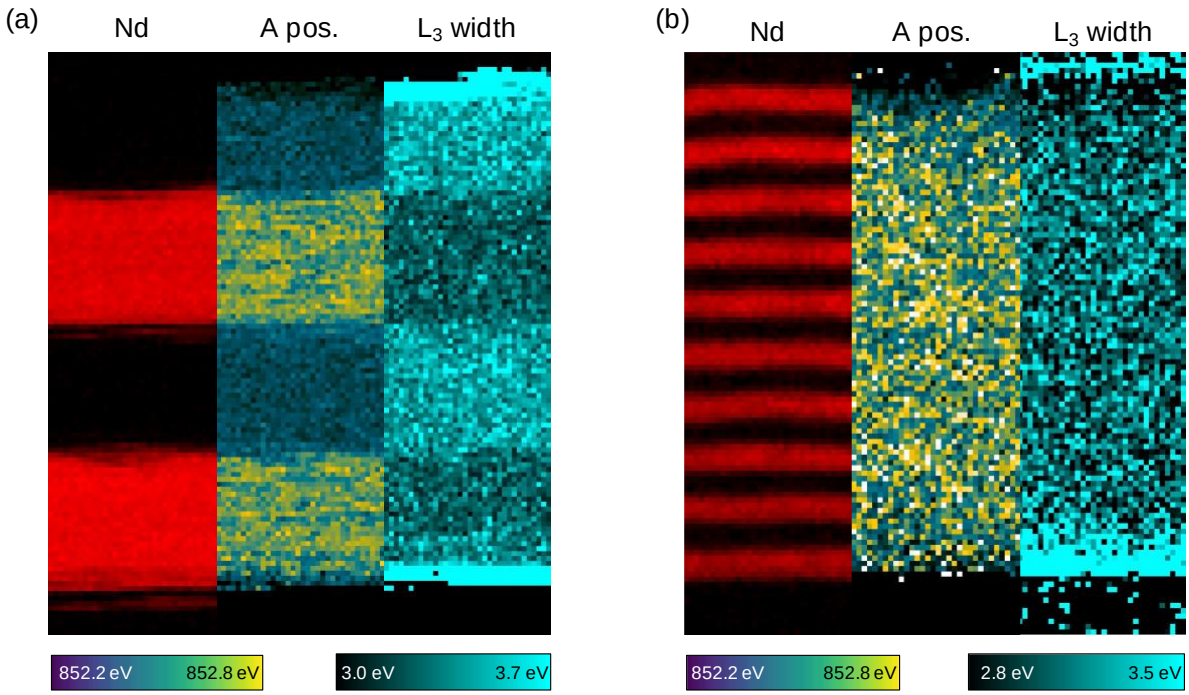


**Figure S4.** From left to right: Maps showing the Nd composition, the shift of peak A and the width of the Ni $L_3$ peak obtained from the (a) $(30,30)_2$ and (b) $(5,5)_{10}$ SLs.

## References:


(1) Peña, F. de la; Prestat, E.; Fauske, V. T.; Burdet, P.; Jokubauskas, P.; Nord, M.; Furnival, T.; Ostasevicius, T.; MacArthur, K. E.; Johnstone, D. N.; Sarahan, M.; Lähnemann, J.; Taillon, J.; pquinn-dls; Migunov, V.; Eljarrat, A.; Aarholt, T.; Caron, J.; Mazzucco, S.; Martineau, B.; Somnath, S.; Poon, T.; Walls, M.; Slater, T.; Winkler, F.; Tappy, N.; Donval, G.; Myers, J. C.; McLeod, R.; Hoglund, E. R. Hyperspy/Hyperspy: HyperSpy 1.6.0. **2020**. https://doi.org/10.5281/ZENODO.3973513.

(2) Jones, L.; Wenner, S.; Nord, M.; Ninive, P. H.; Løvvik, O. M.; Holmestad, R.; Nellist, P. D. Optimising Multi-Frame ADF-STEM for High-Precision Atomic-Resolution Strain Mapping. *Ultramicroscopy* **2017**, *179*, 57–62. https://doi.org/10.1016/j.ultramic.2017.04.007.

(3) Jones, L.; Yang, H.; Pennycook, T. J.; Marshall, M. S. J.; Van Aert, S.; Browning, N. D.; Castell, M. R.; Nellist, P. D. Smart Align—a New Tool for Robust Non-Rigid Registration of Scanning Microscope Data. *Adv. Struct. Chem. Imaging* **2015**, *1*, 8. https://doi.org/10.1186/s40679-015-0008-4.

(4) Ahn, C. C.; Krivanek, O. L. *A Reference Guide of Electron Energy Loss Spectra Covering All Stable Elements*; Gatan, I., Ed.; Warrendale, 1983.